

RESEARCH ARTICLE

10.1002/2017JA025163

Special Section:
Mars Aeronomy**Key Points:**

- We simulate the hydrogen density near the exobase of Mars
- We study local time and latitudinal variations of the exospheric hydrogen density at equinox and southern solstice
- The hydrogen distribution at the exobase of Mars is close to Zero Net Ballistic Flux equilibrium

Correspondence to:J.-Y. Chaufray,
jean-yves.chaufray@latmos.ipsl.fr**Citation:**Chaufray, J.-Y., Yelle, R. V., Gonzalez-Galindo, F., Forget, F., Lopez-Valverde, M., Leblanc, F., & Modolo, R. (2018). Effect of the lateral exospheric transport on the horizontal hydrogen distribution near the exobase of Mars. *Journal of Geophysical Research: Space Physics*, 123, 2441–2454. <https://doi.org/10.1002/2017JA025163>

Received 27 DEC 2017

Accepted 9 MAR 2018

Accepted article online 25 MAR 2018

Published online 30 MAR 2018

Effect of the Lateral Exospheric Transport on the Horizontal Hydrogen Distribution Near the Exobase of Mars

J.-Y. Chaufray¹ , R. V. Yelle², F. Gonzalez-Galindo³, F. Forget⁴, M. Lopez-Valverde³, F. Leblanc¹ , and R. Modolo¹ ¹LATMOS/IPSL, UPMC University Paris 06 Sorbonne Universités, UVSQ, CNRS, Paris, France, ²Lunar and Planetary Laboratory, University of Arizona, Tucson, AZ, USA, ³Instituto de Astrofísica de Andalucía, CSIC, Granada, Spain, ⁴Laboratoire de Météorologie Dynamique, IPSL, CNRS, Paris, France

Abstract We simulate the hydrogen density near the exobase of Mars, using the 3-D Martian Global Circulation Model of Laboratoire de Météorologie Dynamique, coupled to an exospheric ballistic model to compute the downward ballistic flux. The simulated hydrogen distribution near the exobase obtained at two different seasons— $L_s = 180^\circ$ and $L_s = 270^\circ$ —is close to Zero Net Ballistic Flux equilibrium. In other words, the hydrogen density near the exobase adjusts to have a balance between the local upward ballistic and the downward ballistic flux due to a short lateral migration time in the exosphere compared to the vertical diffusion time. This equilibrium leads to a hydrogen density n near the exobase directly controlled by the exospheric temperature T by the relation $nT^{5/2} = \text{constant}$. This relation could be used to extend 1-D hydrogen exospheric model of Mars used to derive the hydrogen density and escape flux at Mars from Lyman- α observations to 3-D model based on observed or modeled exospheric temperature near the exobase, without increasing the number of free parameters.

1. Introduction

Light species such as H and He are found with enhanced densities, sometimes called bulges in the cold regions of terrestrial planet thermospheres. Examples include the terrestrial He bulge near the winter pole (Johnson & Gottlieb, 1969; Reber & Hays, 1973), the nighttime and winter pole H enhancement on Earth (Brinton et al., 1975), the nighttime He and H bulges on Venus (Brinton et al., 1980; Niemann et al., 1980; Kumar et al., 1978; Grebowsky et al., 1996; Chaufray et al., 2015), and enhancement in the He distribution in the winter hemisphere on Mars (Elrod et al., 2017). The H distribution on Mars is of particular interest because it has recently been discovered to be highly variable (Chaffin et al., 2014; Clarke et al., 2017), but the spatial and temporal components of the variability are not yet well understood. The escape of H from Mars is believed to be primarily thermal, that is, Jeans escape, and therefore depends exponentially on temperature, which varies strongly over the exobase. The relative variations of density and temperature are critical to understanding the hydrogen escape variability and the spatial asymmetries of the exosphere and its possible effect on the induced magnetosphere (Holmstrom, 2006) and Lyman- α emissions (Chaffin et al., 2015).

The size and location of these exospheric light species density enhancements are controlled by a combination of processes. They occur in low-pressure regions where there is a convergence of horizontal flow. In the diffusively separated thermosphere, the horizontal flow toward the convergence carries an enhanced abundance of lighter species because of their large-scale heights. Following subsidence in the region of the convergence, the horizontal branch of the return flow occurs at deeper pressures, in the well-mixed region of the atmosphere. The result is a buildup of light species in region of subsidence (e.g., Bougher et al., 1999, 2015; Gonzalez-Galindo et al., 2009). This cycle is modified by several other processes. There are vertical fluxes due to molecular diffusion and advection. Horizontal diffusion also occurs but is unlikely to be important for the scales of interest. The escape fluxes of H and He may be significant and may moderate the density enhancements.

The interplay of these processes on Mars has been studied by Chaufray et al. (2015, 2017), who extended the Laboratoire Météorologie Dynamique General Circulation Model (LMD-GCM; Forget et al., 1999; Gonzalez-Galindo et al., 2009) to include atomic and molecular hydrogen, the associated chemistry, vertical diffusion, and Jeans escape. The simulations encompassed the entire atmosphere, from the surface to the exobase, and were extended into the exosphere using Liouville's equation. Chaufray et al. (2015) found that the H density

near the exobase varied by a factor of several hundred with a density maximum near midnight during solstices and near dawn during equinox, due to circulation patterns in the thermosphere. The H escape rate in these simulations varied by a factor of ~ 8 due to seasonal effects with a maximum near northern winter solstice and a factor of ~ 5 due to solar cycle effects. The dependence of the H escape rate on solar EUV irradiance shows that the escape rate is not diffusion limited but rather controlled by the distribution of exospheric temperature.

The H escape flux calculated by Chaufray et al. (2015) varies by roughly a factor of 1,000 over the exobase. There is a maximum in the early morning and near the polar regions where temperatures are rising but the H bulge has not yet dissipated. In fact, the region of high H escape rates occupies an area of tens of degrees near the poles and tens of degrees near dawn. The fact that these regions of large H escape flux are so sharp emphasizes the need to understand the horizontal shape of the H bulge. This subject is considered in this paper.

The flow of light species (H and H₂) through the exosphere may be strong, and some authors have considered this to be the dominant process controlling the distribution of H at the exobase (Donahue & McAfee, 1964). The Zero Net Ballistic Flux (ZBNF) condition assumes that the time constant for ballistic transport is much shorter than the time constant for advection or diffusion in the thermosphere with the result that the exobase temperature completely defines the H density. Analytic approximations based on this assumption lead to the well-known $nT^{5/2} = \text{constant}$ relationship between H density and temperature at the exobase (Hodges & Johnson, 1968). The justification for the ZBNF condition is rather weak, however, as molecular diffusion times should asymptotically approach exospheric transport times near the exobase. Moreover, the net flux in the region of the density enhancements cannot be zero; instead, the combination of advective and diffusive fluxes in the thermosphere must match the imbalance of ballistic fluxes at the exobase. A rigorous description of light species in a planetary thermosphere must balance all these fluxes. Therefore, we have developed a model that fully couples the circulation of the atmosphere with ballistic flow in the exosphere.

2. Modeling of the Lateral Transport

2.1. Description of the Ballistic Code

In this study, we consider hydrogen atoms to have ballistic trajectories above the upper level of the LMD-GCM. The upper level of the LMD-GCM is the isobar surface $P = 10^{-8}$ Pa.

This level does not correspond exactly to the exobase (where the Knudsen number is equal to 1), but we still use “exobase” to name this upper level. The pressure at the exobase can be estimated from the equality between the scale height and the mean free path leading to $P_{\text{exo}} = mg/\sigma$ where m is the mean molecular mass, g the gravitational acceleration, and σ the collisional cross section. For typical value of collisional cross section between H and O $\sigma = 3 \times 10^{-15}$ cm² (Lewkow & Kharchenko, 2014) and a mean molecular mass $m = 2.66 \times 10^{-26}$ kg, we found $P_{\text{exo}} \sim 3 \times 10^{-7}$ Pa, below the upper level of the GCM-LMD. Because the main parameters (temperature and hydrogen density) used in this study vary slowly vertically at these altitudes, using another pressure for the upper level should not change our conclusions.

The ballistic code used in these simulations is a kinetic model, computing the downward ballistic flux at any location at the upper level from

$$\Phi_{\text{dw}}(\theta, \varphi, t) = \int_{V=0}^{V=V_{\text{esc}}} \int_{\theta_v=-\pi/2}^{\theta_v=0} \int_{\varphi_v=0}^{\varphi_v=2\pi} V^3 f(V, \theta_v, \varphi_v, \theta, \varphi, t) \cos\theta_v \sin\theta_v dV d\theta_v d\varphi_v \quad (1)$$

where V , θ_v , and φ_v are the magnitude of the velocity, the angle between the velocity vector and the local horizontal plane, and the azimuthal angle of the velocity vector of the ballistic particles moving downward, respectively, and θ and φ are the latitude and longitude of the position at the exobase.

In this model, we neglect all collisions above the upper level and therefore use the Liouville’s theorem.

Consequently, the value of the velocity distribution function (VDF) remains constant along a dynamical trajectory and, for downward directed atoms, is related to the value of the VDF at ejection positions $f(V_0, \theta_0, \varphi_0, t_0)$ connected by the orbit (e.g., Vidal-Madjar & Bertaux, 1972):

$$f(V, \theta_v, \varphi_v, \theta, \varphi, t) = f(V_0, \theta_{v,0}, \varphi_{v,0}, \theta_0, \varphi_0, t_0) \quad (2)$$

We assume the upper level to be spherical, which is not correct because the upper level in the GCM is defined as an isobar surface, which is not spherical due to nonuniform temperatures at the exobase and composition in the thermosphere and atmosphere below. However, because the scale height of atomic hydrogen (~ 500 km) is much larger than the altitude variations of the top of the GCM (few tens of kilometers at most between dayside and nightside), this approximation should be quite accurate. The neutral winds near the exobase are also neglected. Horizontal winds can reach a few hundreds of m/s and large-scale vertical winds only a few m/s (e.g., Gonzalez-Galindo et al., 2009), while the thermal velocity of atomic hydrogen is typically ~ 1.8 km/s at 200 K. Therefore, the effect of the thermospheric winds should be small for atomic hydrogen.

The photoionization lifetime can be estimated from the photoionization frequency from Huebner et al. (1992). For current solar conditions, this frequency, rescaled to the Sun-Mars distance, is between 0.3 and $0.8 \times 10^{-7} \text{ s}^{-1}$ and therefore the typical lifetime of an exospheric hydrogen atom is > 115 days. The charge exchange ionization frequency estimated by Chen and Cloutier (2003) is at most 1 order of magnitude larger ($\sim 5 \times 10^{-7} \text{ s}^{-1}$), consistent with the escape rate ratio of H^+ produced by charge exchange and photoionization computed by Modolo et al. (2005). This ionization frequency leads to a lifetime of ~ 20 days. This time is still much larger than the ballistic time of most of the atoms (few hours), and therefore, only a negligible fraction of hydrogen atoms should be lost by ionization. The ionization by photoelectron impact should be small compared to photoionization and charge exchange (Modolo et al., 2005). The effect of radiation pressure should be also important only for the ballistic particles with a long traveltime representing only a small fraction of the ballistic hydrogen atoms. Because all collisions are neglected, we do not consider the collisions between hydrogen atoms and the hot oxygen population formed by O_2^+ dissociative recombination (e.g., Leblanc et al., 2017). These few collisions could increase the escape rate and therefore reduce the ballistic downward flux. But the escape rate was shown to be small compared to thermal escape by Krasnopolsky (2010), and therefore, these collisions are neglected in this study.

Assuming a Maxwellian-Boltzmann distribution for the particles leaving the upper level, the right term of equation (2) can be computed using the density $n(\theta_0, \varphi_0)$ and the temperature $T(\theta_0, \varphi_0)$. The integral is computed using a Gaussian-Legendre method. The comparison of our model with the theory of Hodges and Johnson (1968) is presented in the appendix. The real distribution at the exobase should differ from a Maxwellian distribution. Due to the escaping particles, the Maxwellian distribution should be truncated at velocity larger than the escape velocity (Terada et al., 2016). However, this truncation should not affect the ballistic distribution with a velocity lower than the escaping velocity but only reduce the escape rate (Brinkmann, 1970). The Direct Simulation Monte Carlo method used by Terada et al. (2016) shows that the ballistic hydrogen population is very close to the Maxwellian distribution at the local temperature (see their Figure 8b).

2.2. Temporal Discretization

Conditions near the exobase vary with time, and it takes some time for ballistic atoms to travel from one point on the exobase to another. To take into account this noninstantaneous travel, we discretize the downward flux in time $F_t(i)$, corresponding to atoms leaving the exobase at t and coming back to the exobase between $t + (i - 1)dt$ and $t + idt$ by

$$F_t(i) = \int_{V=0}^{V=V_{esc}} \int_{\theta_v=-\pi/2}^{\theta_v=0} \int_{\varphi_v=0}^{\varphi_v=2\pi} V^3 f(V, \theta_v, \varphi_v, \theta, \varphi, t) \cos\theta_v \sin\theta_v \Pi((i - 1)dt, idt) dV d\theta_v d\varphi_v \quad (3)$$

where $\Pi((i - 1)dt, idt)$ is the box function equal to 1 if the flight time of the ballistic particles $\tau(V_0, \theta_{v,0})$ is between $(i - 1)dt$ and idt and zero elsewhere. For example, $F_t(1)$ correspond to particles with an exospheric traveltime $\tau < dt$, that is, particles leaving and coming back to the exobase instantaneously in the simulation.

The exospheric traveltime τ is the time of the motion above the upper level. The trajectory of any ballistic particle above the exobase is a portion of ellipse (Figure 1) with Martian center as one focal point. The apocenter is in the exosphere and the pericenter below the exobase. The exospheric traveltime can be estimated from the fictive motion along the full ellipse and is given by $\tau = P - 2|t - t_p|$, where P is the period along the ellipse and $|t - t_p|$ is the time between the periapsis and the exobase (Figure 1) given by $|t - t_p| = |E - \text{esin}E|/n$ with $n = 2\pi/P$ (e.g., Capderou, 2005). Therefore, the exospheric traveltime is given by

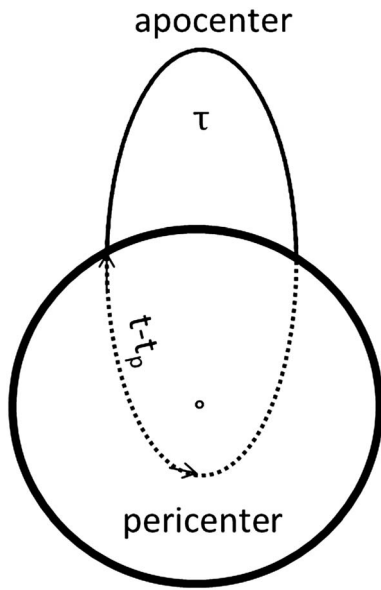


Figure 1. Geometry of one ballistic trajectory in the exosphere (solid line of the ellipse); the exobase is represented by the circle, and the dotted line represents the extrapolation of the elliptical trajectory below the exobase. Because of collisions below the exobase, this dotted line is not the real trajectory of the atom.

$$\tau = P \left[1 - \frac{1}{\pi} |E - e \sin E| \right] \quad (4)$$

where e is the eccentricity of the orbit of the particle, E the eccentric anomaly at the exobase, and P the period of the orbit. E , e , and P depend on V_0 and $\theta_{v,0}$ only.

The downward flux at a given position and a given time t is therefore the combination of the flux of particles leaving the exobase at time lower than t : $\{F_{t-(i-1)\Delta t}\}_{i=1, \dots, l}$

$$\Phi_{dw}(\theta, \varphi, t) = \sum_{i=1}^{i=l} F_{t-(i-1)\Delta t}(i) \quad (5)$$

Here we limit the sum at $i = l = 1,000$, so $i \in [1, \dots, l]$. We assume that all particles with a traveltime larger than $l\Delta t$ (6.25 hr) reach the exobase at $l\Delta t$. We choose $l\Delta t$ large enough in order to have a small contribution of the last term of the sum $F_{t-(i-1)\Delta t}(l)$ to the downward flux. As discussed above, loss by ionization (photoionization, solar wind electron impact, or proton charge exchange) is negligible for current solar conditions but could be possibly taken into account (for example, to study periods of stronger EUV solar flux) by deriving l from the ionization lifetime and without considering atoms with a traveltime larger than $l\Delta t$. The effect of radiation pressure (e.g., Beth et al., 2016) is also neglected in this study.

3. Coupling With the GCM

3.1. Short Description of the GCM-LMD

The Global Circulation Model of the Laboratoire de Météorologie Dynamique (GCM-LMD) is a 3-D model of the Martian atmosphere from the surface to the exobase. It is composed of a 3-D dynamics core solving the fluid equations over a sphere and a physical core describing all the physical processes computed for each column. In all the simulations presented below, the horizontal resolution is 5.625° in longitude and 3.75° in latitude. The dynamical time step δt is 1 sol/960. ~ 1.5 min, and the physics time step is $\Delta t = 5\delta t \sim 7.5$ min. More details on the GCM-LMD can be found in Forget et al. (1999) and Gonzalez-Galindo et al. (2009, 2015).

3.2. Coupling the Ballistic Model to the GCM

In the GCM, when solving the molecular diffusion of each species, an upper boundary is needed for the vertical velocity. In Chaufray et al. (2015), we used a zero vertical velocity at the model top for most of the species except H and H_2 for which we used the local Jeans velocity or effusion velocity. This assumption is correct only if the ZNBF condition is fulfilled, which was not the case in Chaufray et al. (2015).

In the simulations presented here, the H vertical velocity at the top is now computed by

$$w_{top} = \frac{\Phi_{up} - \Phi_{dw}}{n} \quad (6)$$

The local upward flux is the sum of the local escape flux $\Phi_{up,esc} = n w_{eff}$ and upward ballistic flux $\Phi_{up,bal}$ and is given by

$$\Phi_{up} = \Phi_{up,esc} + \Phi_{up,bal} = \frac{nV}{4} = \frac{nU}{2\sqrt{\pi}} \quad (7)$$

where $\langle V \rangle = (8kT\pi/m)^{1/2}$ and $U = (2kT/m)^{1/2}$ depends on the local temperature T . n is the local density, and k is the Boltzmann's constant. The downward flux Φ_{dw} is computed using the ballistic model presented in section 2.

Since we assume no loss other than Jeans escape, the hydrogen atoms leaving the exobase with a velocity lower than the escape velocity should come back to the exobase. To numerically conserve these hydrogen atoms, the net velocity is rescaled to have an integrated (over the exobase surface) downward flux equal

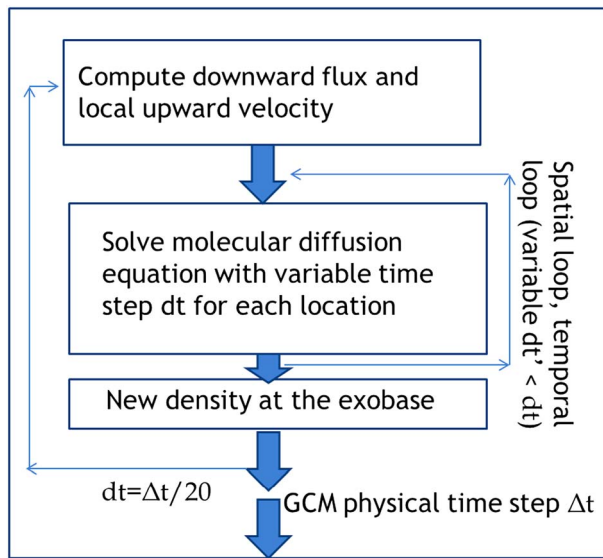


Figure 2. Schematic view of the temporal coupling between the molecular diffusion and the exospheric ballistic transport in the LMD-GCM.

We have found that a small time step is required to couple molecular diffusion to ballistic flow. Indeed, if the time step is too large, a numerical instability can be produced: For example, if the derived vertical velocity at a given position is negative, the hydrogen density at the top will increase, and the upward flux at the next time step will increase (equation (4)). This upward flux can become larger than the downward flux and, in that case, the vertical velocity at the upper boundary will be positive (equation (3)). A positive vertical velocity will lead to a decrease of the hydrogen density at the top and the upward flux at the next time step will decrease, leading possibly to a negative velocity again. If the time step is too large, this oscillation can be unstable. The temporal scheme of the numerical coupling is displayed in Figure 2.

In these simulations the physical time step of the GCM is $\Delta t = 7.5$ min. The time step used to compute the downward flux is $dt = \Delta t/20$. The largest time flight considered for the temporal discretization (ldt) of the downward flux is $1,000dt = 50\Delta t$ (~6.25 hr). The boundary condition used to solve the molecular diffusion

is then derived, and the molecular diffusion is solved using another time step dt' depending on the local conditions, lower than dt , and the final hydrogen density is used to compute the downward flux at the next time step; the loop is done for the 20 sub-time steps. We simulate five Martian days for all cases presented in the next section. The results are presented for one given time step (noon is at longitude 0°) of the last simulated Martian rotation. Using other Martian days or other universal time will not change the conclusion of the paper. We simulate the hydrogen density at the exobase for two seasons: equinox ($L_s = 180^\circ$) and northern winter solstice ($L_s = 270^\circ$), assuming a mean solar activity scenario similar to Chaufray et al. (2015).

$$w_{\text{top}} = \frac{K\Phi_{\text{up}} - \Phi_{\text{dw}}}{n} + (1 - K)w_{\text{eff}} \quad (8)$$

with

$$K = \frac{\int_{\text{exobase}} \Phi_{\text{dw}} ds}{\int_{\text{exobase}} \Phi_{\text{up,bal}} ds} \quad (9)$$

where the integration is over the exobase surface.

Using these two equations, it is straightforward to show that numerically, we have

$$\int_{\text{exobase}} nw_{\text{top}} dS = \int_{\text{exobase}} nw_{\text{eff}} dS \quad (10)$$

And therefore the numerical net loss of hydrogen atoms over the full exobase surface (left term of equation (10) is equal to the global Jeans escape flux (right term of equation (10)).

Most of the time (except at the first time steps), K is close to 1, and equation (8) is close to equation (6).

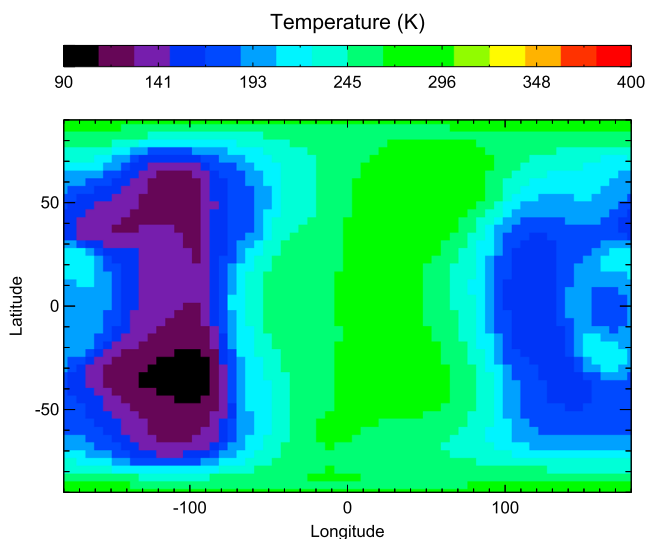


Figure 3. Temperature near the exobase at $L_s = 180^\circ$. In this figure, noon is at longitude 0° and midnight at longitude 180° .

4. Results at Equinox $L_s = 180^\circ$

The temperature distribution at the exobase obtained for the simulations at $L_s = 180^\circ$ is displayed in Figure 3. This map is not very different between the simulations with and without the ballistic transport of hydrogen atoms in the exosphere as expected.

At this season, the exospheric temperature simulated with the GCM-LMD presents a dawn/dusk asymmetry with a minimal temperature at the night morning side (Chaufray et al., 2015). The atomic hydrogen density

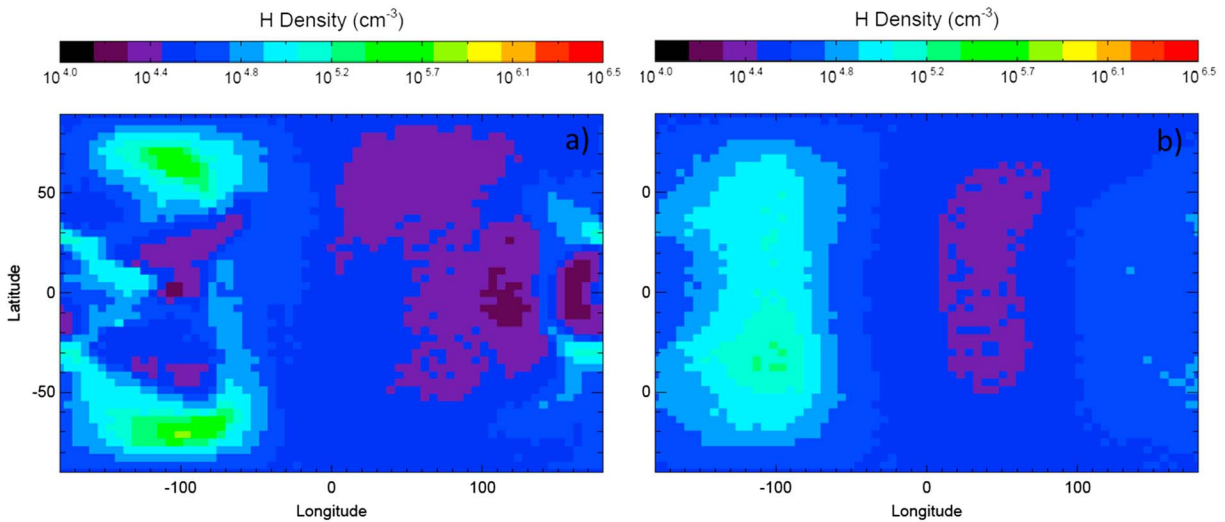


Figure 4. Atomic hydrogen density at the Martian exobase simulated by the LMD-GCM at $L_s = 180^\circ$ (a) without coupling with the exospheric ballistic transport and (b) coupled with the exospheric ballistic transport.

obtained for the simulations without and with ballistic transport of hydrogen atoms in the exosphere is displayed in Figure 4. At $L_s = 180^\circ$, the hydrogen density at the exobase without ballistic transport presents two large spots at latitudes about $\pm 70^\circ$ (Figure 4a) as already shown in Chaufray et al. (2015). These two maxima merge when the ballistic transport is included (Figure 4b). In this last case, the dawn “bulge” is extended at all latitudes. As shown in Figure 4b, the main effect of the ballistic transport in the exosphere is to reduce the horizontal density gradient, increasing the density at the dayside and decreasing the density at the nightside.

When the exospheric ballistic transport is taken into account (Figure 4b), we can see a strong anticorrelation with the temperature at the exobase (Figure 3). The hydrogen density is maximum in the region of the lowest temperature as expected from the Hodges and Johnson (1968) theory. This anticorrelation will be further discussed in section 6.

The Jeans escape flux for these simulations is displayed in Figure 5. When the ballistic transport is not included, the maps are similar to those published by Chaufray et al. (2015), with some differences due to the monthly average presented in Chaufray et al. (2015) compared to the instantaneous map shown in this

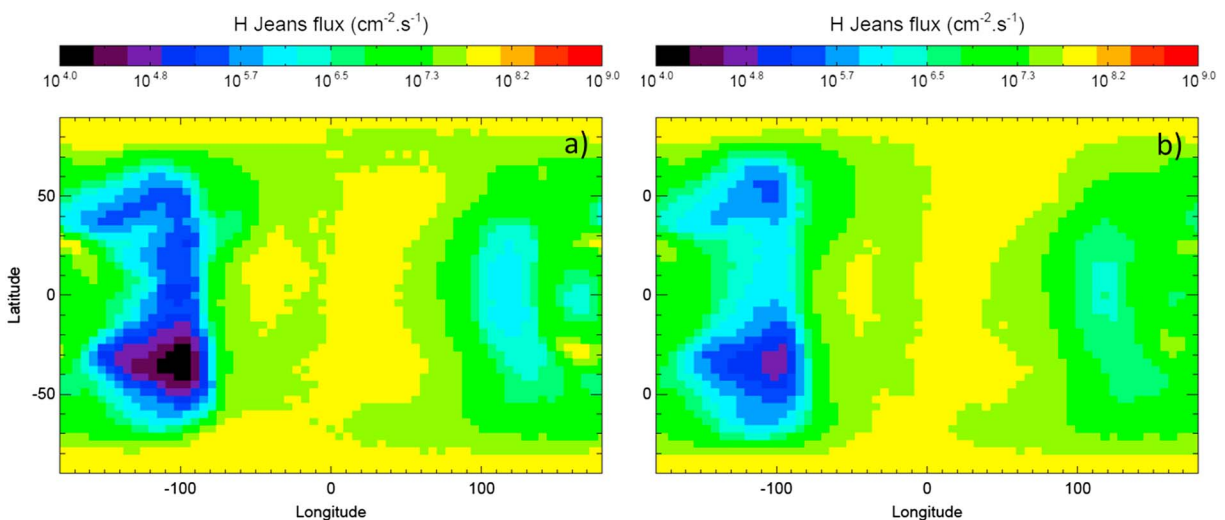


Figure 5. Atomic hydrogen Jeans escape flux at the Martian exobase simulated by the LMD-GCM at $L_s = 180^\circ$ (a) without coupling with the exospheric ballistic transport and (b) coupled with the exospheric ballistic transport.

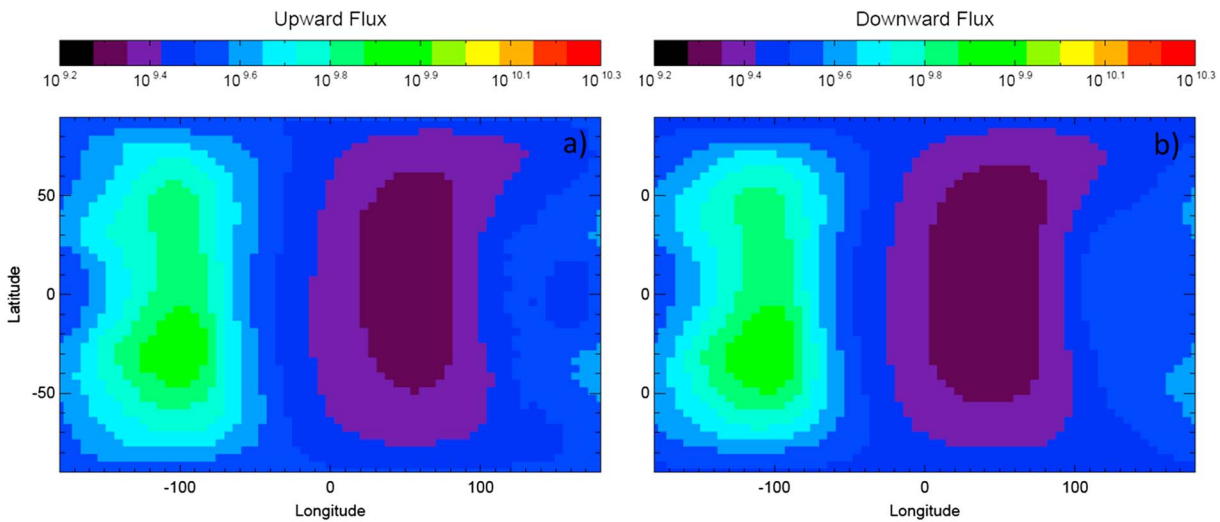


Figure 6. Atomic hydrogen (a) upward flux and (b) downward flux at the Martian exobase simulated by the LMD-GCM, coupled to the ballistic transport model at $L_s = 180^\circ$. The color scale is a \log_{10} scale of the flux in atom per cm^2/s .

paper. The escape fluxes in these two simulations are similar and correlated with the temperature. The global escape rate is $\sim 5 \times 10^{25} \text{ s}^{-1}$, similar to Chaufray et al. (2017) at this season.

The upward and downward fluxes at the exobase, computed from the hydrogen density and temperature distributions obtained when coupling the LMD-GCM to the ballistic transport model, are displayed in Figure 6. The global distribution at the exobase of the downward and upward fluxes is similar to the hydrogen density. The variation of the upward flux is $nT^{1/2}$ (equation (7)). The temperature varies by a factor ~ 3 (Figure 3) and the density at the exobase by a factor ~ 10 (Figure 4). Therefore, the strong correlation between the upward flux and the hydrogen density is expected. The similar distribution of the upward flux and the downward flux indicates that the hydrogen density at the exobase should be close to the ZNBF equilibrium.

The map of the net flux (Figure 7) is different and closer to the temperature map and the Jeans escape map (Figure 5) as expected from the ZNBF equilibrium. Indeed, the Jeans escape flux depends exponentially on the temperature and linearly on the hydrogen density.

Unfortunately, the net flux corresponds to the difference of two large numbers (equation (6)), and the net flux is about at least 1 order of magnitude lower than the upward and downward fluxes; therefore, it is difficult to know if the disagreement between the net flux and the theoretical Jeans escape flux is physical or a numerical result strongly model dependent. The fact that the net flux distribution is close to the Jeans escape flux in our simulation seems to indicate that the ZNBF is probably a good assumption on Mars at first order at equinox. This point will be discussed in more details in section 6. The main region where the net flux differs from the Jeans flux is at the morning terminator where the temperature gradients are strongest. The dayside morning net flux is upward and the dayside net flux, while the net flux is generally weakly downward at the nightside, with minima correlated to the temperature minima.

The local time variations of the hydrogen density at different altitudes at the equator are given in Figure 8 for the two simulations. Noon is at longitude 0° as in the maps presented above. Using another universal time will not change the conclusion since all the structures presented here are associated to local time and not at a specific longitude.

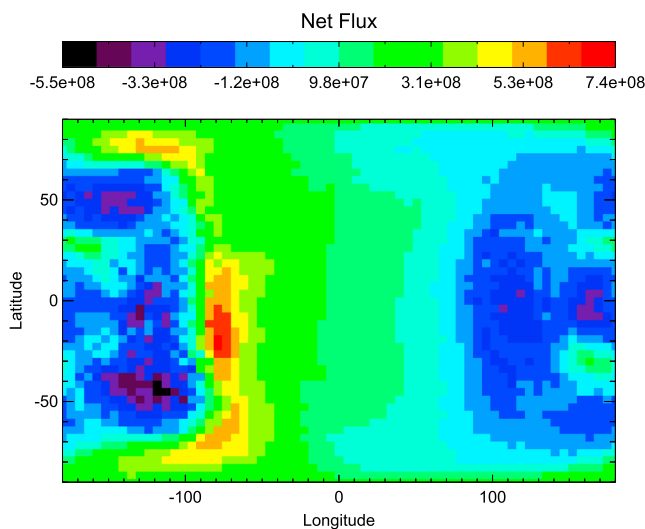


Figure 7. Atomic hydrogen net flux at the Martian exobase simulated by the LMD-GCM, coupled to the ballistic transport model at $L_s = 180^\circ$, derived from the difference between Figures 6a and 6b. The color scale is a \log_{10} scale of the flux in atom per cm^2/s .

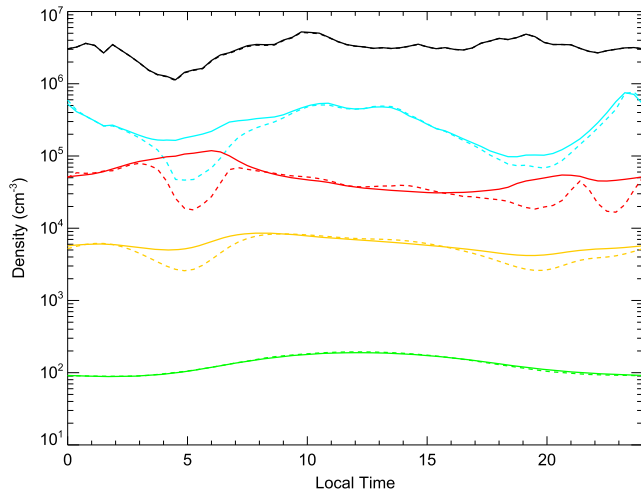


Figure 8. Local time variations of the hydrogen density at different altitudes and for latitude = 0° for the simulation with ballistic coupling (solid lines) and without ballistic coupling (dashed lines) at Ls = 180°. From top to bottom, the altitudes of the profiles are at 80 km (black), 120 km (blue), 260 km (red), 1,800 km (orange), and 10,000 km (green). Each local time is associated to a different longitude (as in the maps presented below); noon (LT = 12 hr) is at longitude 0°.

the homopause. A detailed study of this dynamical effect is deferred for a future study, using the helium species, recently included in the LMD-GCM. Near the exobase (260 km), the profiles are consistent with a hydrogen bulge extended toward lower latitudes when the ballistic transport is included and with smoother variations with local time. At high altitudes (10,000 km), the profiles are similar to those published by Chaufray et al. (2015), where the hydrogen density is larger on the dayside, with small variations with local time. Both simulations lead to similar variations, because at high altitude, the hydrogen density is less sensitive to local conditions and is determined primarily by the global mean conditions at the exobase.

5. Results at Solstice Ls = 270°

The temperature distribution at the exobase obtained for the simulations at Ls = 270° is displayed in Figure 9. This map is not very different between the simulations with and without the ballistic transport of hydrogen atoms in the exosphere.

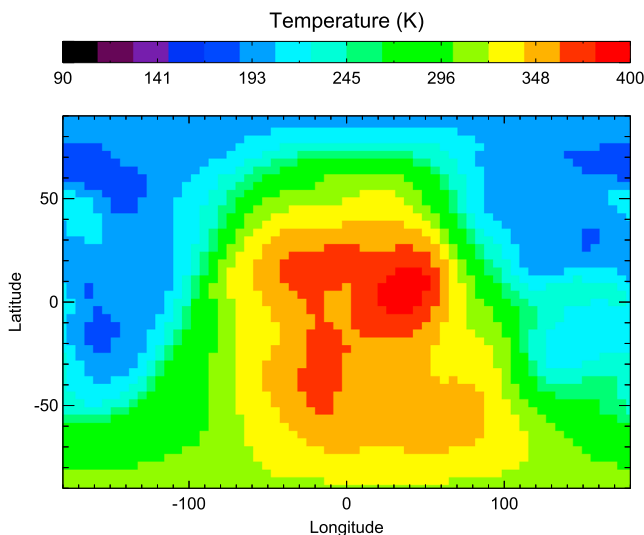


Figure 9. Temperature near the exobase at Ls = 270°. In this figure, noon is at longitude 0° and midnight at longitude = 180°.

To extend the hydrogen density at higher altitudes above the GCM upper level, we use another exospheric model, also based on the Liouville equation in a one way coupling approach. The temperature and hydrogen density computed with the GCM, for the last simulated rotation and with noon at longitude = 180° presented before, is interpolated to the sphere at 200 km altitude (below the GCM upper level). Then, we calculate the variation of density above 200 km, using the algorithm of Vidal-Madjar and Bertaux (1972) as done by Chaufray et al. (2015). The algorithm of Vidal-Madjar and Bertaux is based on the same assumptions and the same formalism as the ballistic code, and therefore, the one-way coupling approach for this extension should be self-consistent. At altitudes above 200 km and below the GCM upper level, the hydrogen density computed with this exospheric model does not differ from the GCM-computed densities.

In the upper mesosphere (~80 km), the hydrogen density is not modified after five simulated days, due to the slow diffusion time in these regions where molecular diffusion is not important. At 120 km, the hydrogen density near terminators at local time (LT) = 5 hr and local time = 19 hr, corresponding to the hydrogen bulge regions, differs substantially in the two simulations. The perturbation produced by the ballistic transport can propagate down to lower altitudes near

the homopause. A detailed study of this dynamical effect is deferred for a future study, using the helium species, recently included in the LMD-GCM. Near the exobase (260 km), the profiles are consistent with a hydrogen bulge extended toward lower latitudes when the ballistic transport is included and with smoother variations with local time. At high altitudes (10,000 km), the profiles are similar to those published by Chaufray et al. (2015), where the hydrogen density is larger on the dayside, with small variations with local time. Both simulations lead to similar variations, because at high altitude, the hydrogen density is less sensitive to local conditions and is determined primarily by the global mean conditions at the exobase.

At this season, the dawn/dusk asymmetry is reduced compared to equinox, and the maximum temperature is at the afternoon as observed by MAVEN/NGIMS (Stone et al., 2016). The important north/south asymmetry is due to the Martian inclination. As for section 4, this map is a snapshot at one given time and therefore should differ from average maps presented by Gonzalez-Galindo et al. (2015) or Chaufray et al. (2015).

The hydrogen density near the exobase obtained for simulations with and without ballistic coupling is displayed in Figure 10.

The day/night asymmetry, noticed by Chaufray et al. (2015), is obtained for both simulations, anticorrelated to the temperature (Figure 9), with a hydrogen bulge at the nightside. A small dawn/dusk asymmetry is still present but much reduced compared to equinox. A dusk/dawn asymmetry of the hydrogen corona has been observed by MAVEN/IUVS at this season (Chaffin et al., 2015). Since the hydrogen density at the exobase is strongly controlled by the temperature at the exobase, a larger dawn/dusk hydrogen asymmetry could result from a larger dawn/dusk asymmetry of the temperature than simulated with the LMD-GCM. But the comparison

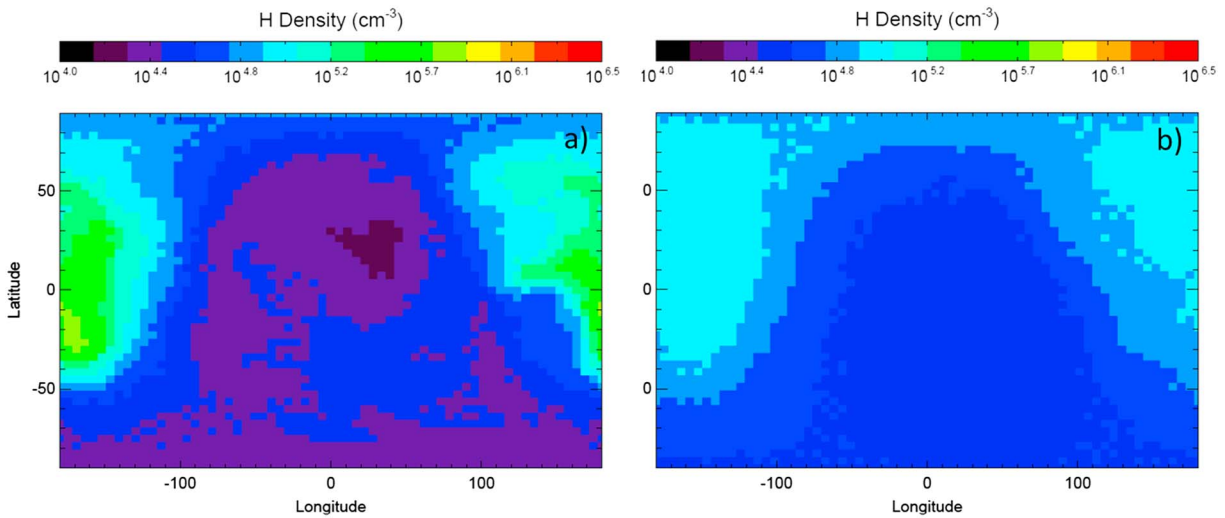


Figure 10. Atomic hydrogen density at the Martian exobase simulated by the LMD-GCM at $L_s = 270^\circ$ (a) without coupling with the exospheric ballistic transport and (b) coupled with the exospheric ballistic transport.

between these maps and the H coronal observations should consider the density at higher altitudes too. A systematic comparison of our simulations and H coronal observations will be presented in the future. The horizontal distribution of the hydrogen density at the exobase is similar for both simulations. The main difference between the simulation with the ballistic transport and the simulation without ballistic transport is the decrease of the bulge hydrogen density at the nightside and the increase of the hydrogen density at the dayside when the ballistic transport is included.

The Jeans escape flux for these simulations is displayed in Figure 11.

When the ballistic transport is not included, the maps are similar to those published by Chaufray et al. (2015), with some differences due to the monthly average presented in Chaufray et al. (2015) compared to the instantaneous map shown in this paper. Some bulges on the Jeans escape flux associated to hydrogen density bulges in the nightside for the simulation without ballistic transport are strongly reduced when the ballistic transport is included. In this last case, similarly to the results obtained at $L_s = 180^\circ$, the escape fluxes are similar to the map of the temperature at the exobase (Figure 9). The global escape rate is $\sim 2 \times 10^{26} \text{ s}^{-1}$ similar to Chaufray et al., 2017 at this season. As for $L_s = 180^\circ$, the maps of the ballistic downward and upward flux are similar and follow the hydrogen density maps (Figure 12).

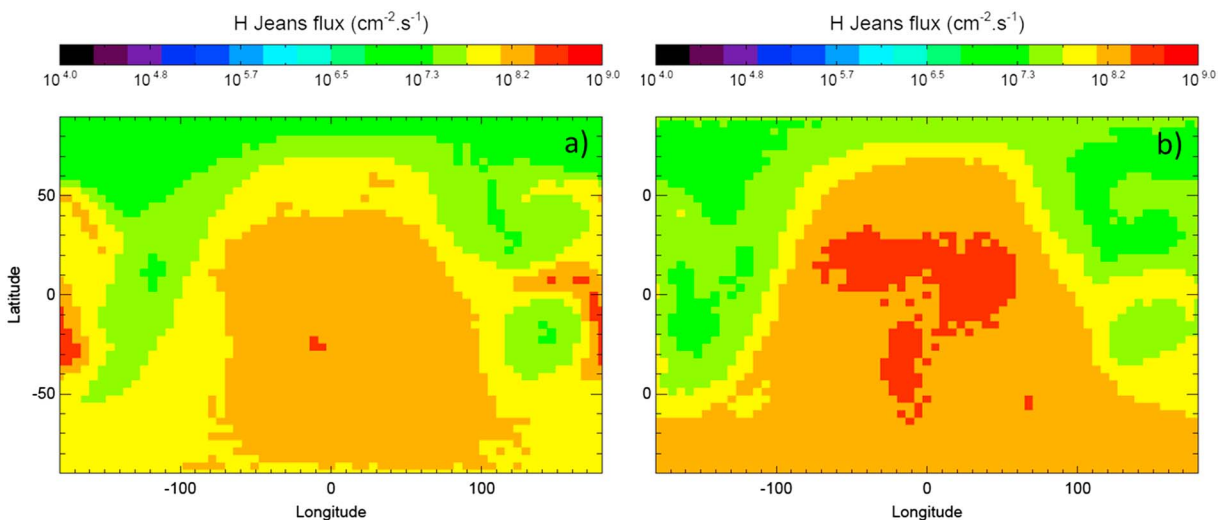


Figure 11. Atomic hydrogen Jeans escape flux at the Martian exobase simulated by the LMD-GCM at $L_s = 270^\circ$ (a) without coupling with the exospheric ballistic transport and (b) coupled with the exospheric ballistic transport.

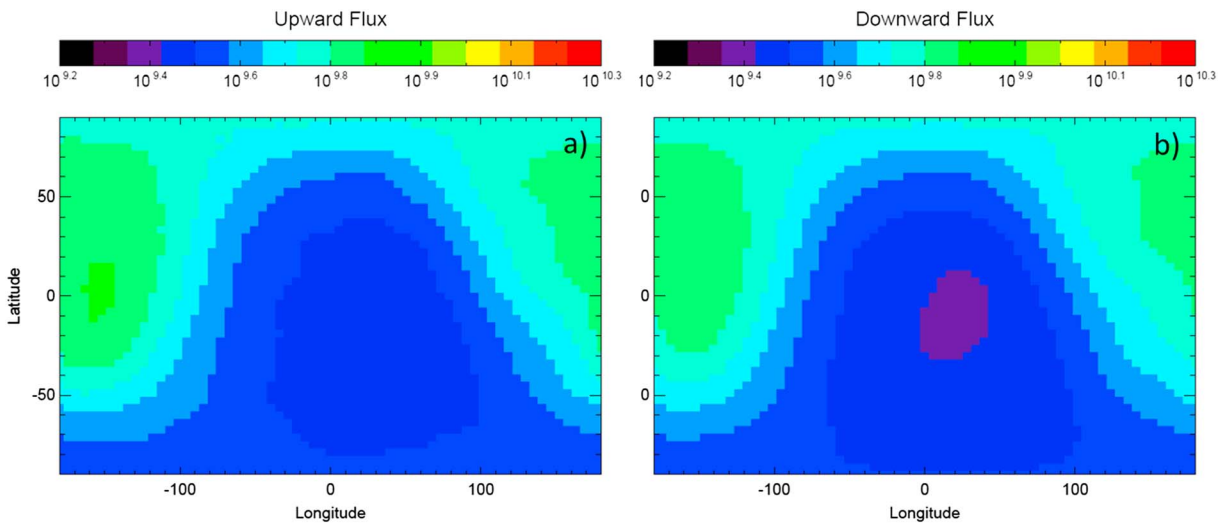


Figure 12. Atomic hydrogen (a) upward flux and (b) downward flux at the Martian exobase simulated by the LMD-GCM, coupled to the ballistic transport model at $L_s = 270^\circ$. The color scale is a \log_{10} scale of the flux in atom per cm^2/s .

The map of the net flux is displayed in Figure 13. The flux is more than 1 order of magnitude lower than the ballistic fluxes. This horizontal distribution is also different from both upward and downward ballistic fluxes. The flux is generally larger at the dayside, but with some structures near midnight similar to the structures of the Jeans flux when the ballistic flux is not included (Figure 11a) or to weak features in the temperature map (Figure 9), this distribution seems not to be exactly at ZNBF. The region of negative net flux (net downward flux) is reduced to a small region near dusk and in the polar winter region (north), while the stronger upward flux is near midnight and at the dayside.

The local time variations of the hydrogen density at different altitudes at the equator are given in Figure 14 for the two simulations.

The simulations lead to the same density below 120 km at $L_s = 270^\circ$. This is different from $L_s = 180^\circ$ due to an increase of the altitude of the homopause at this season in the LMD-GCM, resulting from the expansion of the dusty southern summer hemisphere (Gonzalez-Galindo et al., 2009). The larger amount of hydrogen in the mesosphere at $L_s = 270^\circ$ compared to $L_s = 180^\circ$ is probably due to a larger source of atomic hydrogen by water photodissociation below due to an increase of the hygropause altitude at $L_s = 270^\circ$. A detailed study about the link between the atomic hydrogen and water vapor is deferred to a future work. Near 120 km, a small difference between the two simulations can be observed at the nightside in the region of the bulge. At the exobase, the hydrogen density is larger at the dayside but lower at the nightside when the ballistic transport is included. At very high altitudes (10,000 km), the profiles are similar to those published by Chaufray et al. (2015), where the hydrogen density is larger on the dayside, with very small variations with local time.

At the exobase, the hydrogen density is larger at the dayside but lower at the nightside when the ballistic transport is included. At very high altitudes (10,000 km), the profiles are similar to those published by Chaufray et al. (2015), where the hydrogen density is larger on the dayside, with very small variations with local time.

6. Discussion

For a hydrogen distribution at ZNBF equilibrium, the local density should be related to the temperature at the local exobase by $K_0 = nT^{5/2} = \text{constant}$ (Hodges & Johnson, 1968). K_0 varies by almost 2 orders of magnitude (from $0.27 \times 10^{10} \text{ cm}^{-3}/\text{K}^{2.5}$ to $16.9 \times 10^{10} \text{ cm}^{-3}/\text{K}^{2.5}$), with an average value and a standard deviation of $3.3 \times 10^{10} \text{ cm}^{-3}/\text{K}^{2.5}$ and $1.8 \times 10^{10} \text{ cm}^{-3}/\text{K}^{2.5}$ for the simulation at $L_s = 180^\circ$ without ballistic transport. These values confirm that the density horizontal distribution is far from the ZNBF

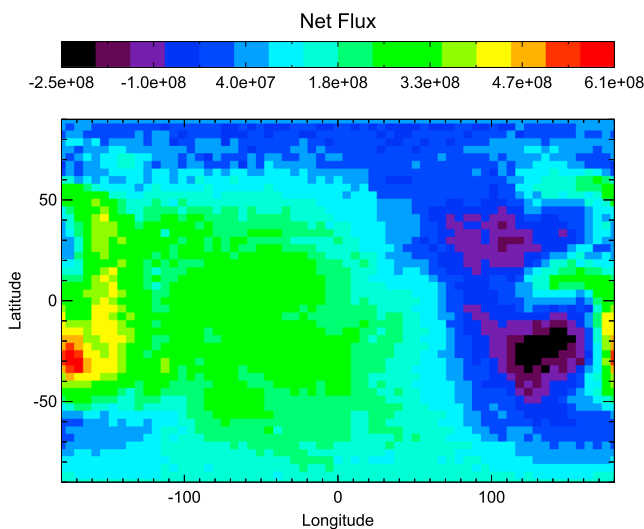


Figure 13. Atomic hydrogen net flux at the Martian exobase simulated by the LMD-GCM, coupled to the ballistic transport model at $L_s = 270^\circ$, derived from the difference between Figures 12a and 12b. The color scale is a \log_{10} scale of the flux in atom per cm^2/s .

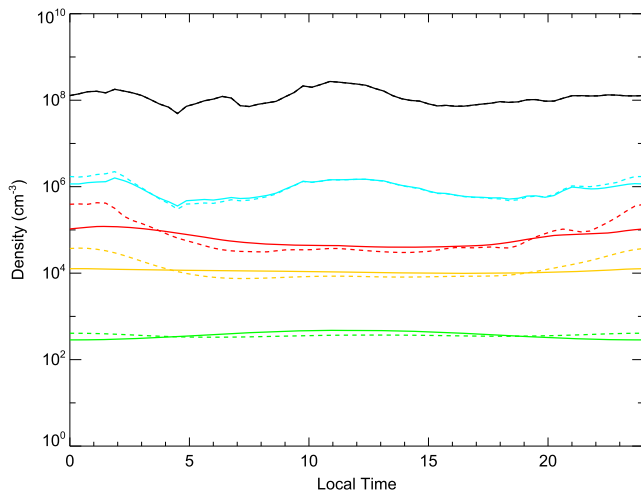


Figure 14. Local time variations of the hydrogen density at different altitudes for the simulation with ballistic coupling (solid lines) and without ballistic coupling (dashed lines) at $L_s = 270^\circ$. From top to bottom, the altitudes of the profiles are at 80 km (black), 120 km (blue), 260 km (red), 1,800 km (orange), and 10,000 km (green).

symmetric models of hydrogen density and observations (e.g., Anderson & Hord, 1971; Bhattacharyya et al., 2015; Chaffin et al., 2014; Chaufray et al., 2008). Three-dimensional models based on a simple sinusoidal parametrization of the temperature and hydrogen density at the exobase have been used for Venus (e.g., Chaufray et al., 2012). The use of the ZNBF relation would reduce the number of free parameters, because in this case, the temperature at the exobase and a constant value for $nT^{2.5}$ are sufficient to provide the complete distribution of the hydrogen density at the exobase. Numerical simulations from GCMs (Bougher et al., 2015; Gonzalez-Galindo et al., 2015) or empirical exospheric temperature maps from MAVEN observations could be considered in the future, and the problem of Lyman- α inversion will be reduced to one free parameter: K_0 (assumptions on the temperature vertical profile is still needed). This new parametrization would be useful to better quantify the latitudinal and local time variability of the Martian hydrogen corona observed by Mars Express (Chaffin et al., 2014; Chaufray et al., 2008), MAVEN (Chaffin et al., 2015), and HST (Bhattacharyya et al., 2015, 2017). The atmospheric sources of hydrogen are not known with accuracy. In particular, a significant amount can be produced by water vapor photodissociation at altitudes well above the hygropause, increasing

equilibrium in this case without ballistic transport. When the ballistic transport is included, the variability of K_0 is strongly reduced; this product varies by less than 1 order of magnitude (from $1.5 \times 10^{10} \text{ cm}^{-3}/\text{K}^{2.5}$ to $5.8 \times 10^{10} \text{ cm}^{-3}/\text{K}^{2.5}$), with an average value and a standard deviation of $3.3 \times 10^{10} \text{ cm}^{-3}/\text{K}^{2.5}$ and $1.0 \times 10^{10} \text{ cm}^{-3}/\text{K}^{2.5}$. The map of this value is displayed in Figure 15. The value is maximal near dawn, where the net flux is maximal, and follows the same variations as the net flux.

At $L_s = 270^\circ$, the variability of K_0 (not shown) is also strongly reduced when the ballistic transport is included. This product varies from $4.1 \times 10^{10} \text{ cm}^{-3}/\text{K}^{2.5}$ to $10.6 \times 10^{10} \text{ cm}^{-3}/\text{K}^{2.5}$, with an average value and a standard deviation of $6.8 \times 10^{10} \text{ cm}^{-3}/\text{K}^{2.5}$ and $1.5 \times 10^{10} \text{ cm}^{-3}/\text{K}^{2.5}$. The distribution follows globally the temperature distribution.

It is difficult to know if the variability is due to numerical uncertainties, but at first order the ZNBF seems to be a reasonable assumption. This is important, because such an assumption could be useful to process and interpret Lyman- α observations of Mars. Numerous derivations of the hydrogen density and escape from the Lyman- α optically thick emission are based on forward comparison between spherically sym-

the hydrogen escape (Chaffin et al., 2017). However, the water vapor mixing ratio there depends on the supersaturation of the upper atmosphere, which is not well known. It has been observed in only a few locations by Spectroscopy for the Investigation of the Characteristics of the Atmosphere of Mars (SPICAM) (Maltagliati et al., 2013). The microphysical processes controlling this supersaturation are now included in the LMD GCM (Navarro et al., 2014), but the results depend on model parameters not well constrained by the observations. Supersaturated water would increase the global amount of hydrogen at the exobase (and therefore K_0) but not necessarily the horizontal distribution of the hydrogen density at the exobase, and therefore, the parametrization presented in this section could be still valid.

The simulations presented in this paper have been done for an arbitrary solar activity and are not appropriate for comparisons with UV observations from Mars Express, MAVEN, or HST. Moreover, the link between these UV emissions and the hydrogen density is not straightforward due to the optical thickness of the Lyman- α emission line (e.g., Chaufray et al., 2008) and requires a 3-D radiative transfer model for resonance line. The exospheric ballistic motion of hydrogen atoms

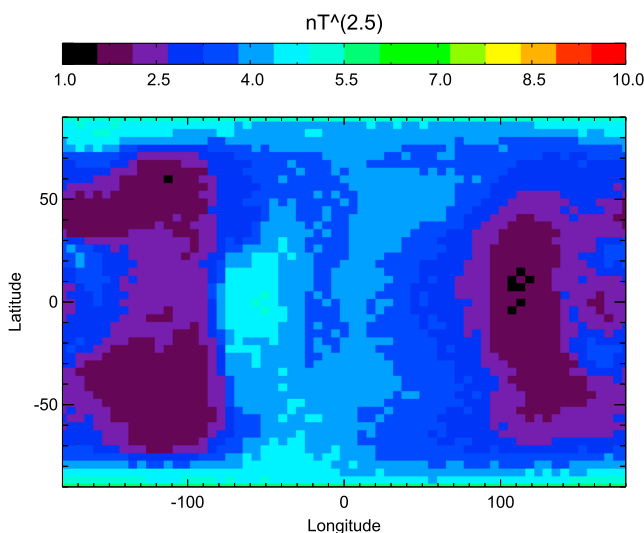


Figure 15. Map of $nT^{5/2}$ near the exobase, for the simulation with the ballistic transport at $L_s = 180^\circ$ (in $10^{10} \cdot \text{cm}^{-3} \cdot \text{K}^{2.5}$).

should exist anyway, and therefore, the possible disagreement between our simulations and observations should not question the process described in this paper but other processes in the GCM, which would lead to discussions beyond the scope of this study.

7. Summary/Conclusion

We couple a ballistic transport model of atomic hydrogen in the exosphere to the Global Circulation Model of the Laboratoire de Météorologie Dynamique (GCM-LMD) to simulate self-consistently the hydrogen density at the exobase of Mars. The ballistic transport model is used to compute the downward flux at the exobase needed to derive the upper boundary condition on the vertical velocity of the molecular diffusion in the GCM-LMD. The flight time in the exosphere is taken into account in this approach. These simulations are done at equinox and northern winter. The hydrogen density is much smoother when this ballistic transport is included compared to our previous simulations without ballistic transport. The hydrogen density is anticorrelated with the temperature at the exobase and can form hydrogen bulge in the regions of low temperature (at nightside dawn at $L_s = 180^\circ$ and nightside at $L_s = 270^\circ$). The results show that the hydrogen density is not too far from the Zero Net Ballistic Flux condition given by the relation $nT^{5/2} = \text{constant}$. This ZNBF relation could be useful to build realistic empirical model of planetary hydrogen corona with few free parameters to interpret numerous observations from Mars Express, HST, and MAVEN. The recent extension of the Venusian GCM of LMD (Gilli et al., 2017) could be also coupled to a ballistic model in the future to investigate the hydrogen bulge on Venus observed by Pioneer Venus Orbiter and more recently by SPICAV/Venus Express. This coupling will be more difficult for Venus, because escape parameter is larger on Venus and therefore the numerical computation of the downward and upward fluxes will need to be more accurate to derive the net flux. Because the escape parameter is larger, we should expect the horizontal redistribution of the hydrogen atoms at the exobase to be less efficient on Venus and therefore the hydrogen bulge stronger on Venus than Mars. Variations of the hydrogen density with local time at the exobase by more than 1 order of magnitude have been deduced on Venus from several observations presented in section 1. On Mars, such variations have not been quantified yet but the first study of latitudinal variations performed from HST (Bhattacharyya et al., 2017) seems to indicate low variations at $L_s = 330^\circ$ above 2.5 Martian radius but larger variations closer to the exobase.

Appendix A: Validation of the Ballistic Code

To validate the code, we compared the net flux obtained for a given distribution of the density and temperature at the exobase with the solution of the horizontal diffusion equation given in Hodges and Johnson (1968), without rotation, assuming a global average escape parameter $\lambda = GMm/kT_0R = 28.6$. Using the notation of Hodges and Johnson (1968), the steady state net flux is given by

$$\Phi = \Phi_2 = \left(1 + \frac{8.4}{\lambda}\right) \nabla_s^2 (nV_{th}H^2)$$

which can be rewritten

$$\Phi = -n \langle V \rangle H^2 \left(1 + \frac{8.4}{\lambda}\right) \frac{1}{nT^{5/2}} \nabla_s^2 (nT^{5/2})$$

This validation has been done by choosing a simple horizontal distribution similar to Hodges and Johnson (1968) given by

$$\begin{aligned} n &= n_0 \exp(C \cos\theta) \\ T &= T_0 \exp[D \sin\theta \cos(\varphi - \varphi_0)] \end{aligned}$$

where θ is the colatitude and φ the longitude, $C = 0.01$, $D = 0.01$, $n_0 = 10^5 \text{ cm}^{-3}$, and $T_0 = 200 \text{ K}$; and $\varphi_0 = \pi$. With these distributions at the exobase, and because $C \ll 1$ and $D \ll 1$, neglecting the second order terms in C and D , after few calculations, the net flux is given by

$$\Phi = K \left[C \cos\theta + \frac{5}{2} D \sin\theta \cos(\varphi - \varphi_0) \right]$$

with

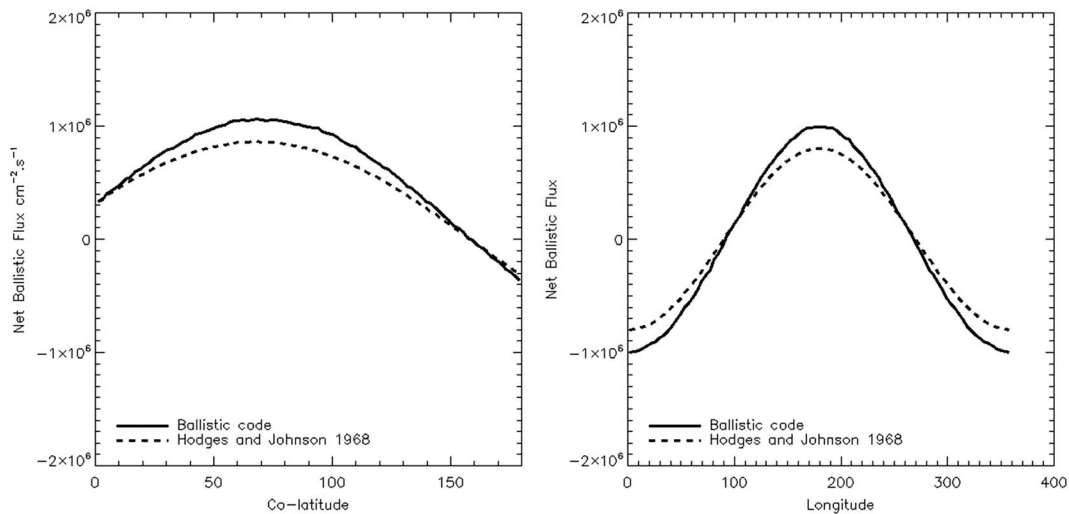


Figure A1. Comparison between the net flux derived from our ballistic model along $\varphi = \pi$ and $\theta = \pi/2$ and the net flux derived from the Hodges and Johnson approximation for the exobase conditions detailed in the text.

$$K = 2n_0 T_0^{5/2} \sqrt{\frac{8k}{\pi m} \frac{k^2 R^2}{m^2 (GM)^2} \left(1 + \frac{8.4}{\lambda}\right)}$$

where k is the Boltzmann constant, m the mass of the species, and R the radius of the exobase (assumed to be a sphere), with the numerical values used in this test, $K = 3.2 \times 10^7 \text{ cm}^{-2}/\text{s}$.

The net fluxes given by this relation along the meridian ($\varphi = \varphi_0 = \pi$) and along the equator ($\theta = \pi/2$) are compared to the net fluxes from our ballistic code in Figure A1. The integral given by equation (1) has been computed using the Gauss-Legendre quadrature with 32, 64, and 16 points for the three integrals over V , θ_v , and φ_v , respectively.

The two equatorial profiles are similar, with differences $\sim 25\%$. These differences are in the range of the differences between the model of McAfee (1967) and the different approximations in Hodges and Johnson (1968) (Figure 4 of Hodges & Johnson, 1968).

Acknowledgments

This project was partly funded by the Programme National de Planetologie and Programme National Soleil Terre and by the Centre National d'Etudes Spatiales. This work has been partially funded by the European Union Horizon 2020 Programme (H2020 Compet-08-2014) under grant agreement UPWARDS-633127. The hydrogen density simulated for the four cases considered in this study can be found at <https://owncloud.latmos.ipsl.fr/index.php/s/4DWm0BMM9BBP756>, <https://owncloud.latmos.ipsl.fr/index.php/s/FD2BKWY89cPR9Tn>, <https://owncloud.latmos.ipsl.fr/index.php/s/GY8J6ITuEJMHVNg>, and <https://owncloud.latmos.ipsl.fr/index.php/s/2Zl4yfwgweEPanu>.

References

- Anderson, D. E., & Hord, C. W. (1971). Mariner 6 and 7 ultraviolet spectrometer experiment: Analysis of hydrogen Lyman- α data. *Journal of Geophysical Research*, *76*, 6666–6673.
- Beth, A., Garnier, P., Toublanc, D., Dandouras, I., & Mazelle, C. (2016). Theory for planetary exospheres: II. Radiation pressure effect on exospheric density profiles. *Icarus*, *266*, 423–432. <https://doi.org/10.1016/j.icarus.2015.08.023>
- Bhattacharyya, D., Clarke, J. T., Bertaux, J.-L., Chaufray, J.-Y., & Mayyasi, M. (2015). A strong seasonal dependence in the Martian hydrogen exosphere. *Geophysical Research Letters*, *42*, 8678–8685. <https://doi.org/10.1002/2015GL065804>
- Bhattacharyya, D., Clarke, J. T., Bertaux, J.-L., Chaufray, J.-Y., & Mayyasi, M. (2017). Analysis and modeling of remote observations of the Martian hydrogen exosphere. *Icarus*, *281*, 264–280. <https://doi.org/10.1016/j.icarus.2016.08.034>
- Bougher, S. W., Engel, S., Roble, R. G., & Foster, B. (1999). Comparative terrestrial planet thermospheres 2. Solar cycle variation of global structure and winds at equinox. *Journal of Geophysical Research*, *104*, 16,591–16,611.
- Bougher, S. W., Pawlowski, D., Bell, J. M., Nelli, S., McDunn, T., Murphy, J. R., et al. (2015). Mars Global Ionosphere-Thermosphere Model: Solar cycle, seasonal, and diurnal variations of the Mars upper atmosphere. *Journal of Geophysical Research: Planets*, *120*, 311–342. <https://doi.org/10.1002/2014JE004715>
- Brinkmann, R. T. (1970). Departures from Jeans' escape rate for H and He in the Earth's atmosphere. *Planetary and Space Science*, *18*(4), 449–478. [https://doi.org/10.1016/0032-0633\(70\)90124-8](https://doi.org/10.1016/0032-0633(70)90124-8)
- Brinton, H. C., Mayr, H. G., & Potter, W. E. (1975). Winter bulge and diurnal variations in hydrogen inferred from AE-C composition measurements. *Geophysical Research Letters*, *2*(9), 389–392. <https://doi.org/10.1029/GL002i009p00389>
- Brinton, H. C., Taylor, H. A., Nieman, H. B., Mayr, H. G., Nagy, A. F., Cravens, T. E., & Strobel, D. F. (1980). Venus night-time hydrogen bulge. *Geophysical Research Letter*, *7*, 865–868.
- Capderou, M. (2005). *Satellites: Orbits and Missions*. Paris: Springer-Verlag.
- Chaffin, M. S., Chaufray, J.-Y., Deighan, J., Schneider, N. M., McClintock, W. E., Stewart, A. I. F., et al. (2015). Three-dimensional structure in the Mars H corona revealed by IUVS on MAVEN. *Geophysical Research Letters*, *42*, 9001–9008. <https://doi.org/10.1002/2015GL065287>
- Chaffin, M. S., Chaufray, J.-Y., Stewart, I. A. F., Montmessin, F., Schneider, N. M., & Bertaux, J.-L. (2014). Unexpected variability of Martian hydrogen escape. *Geophysical Research Letters*, *41*, 314–320. <https://doi.org/10.1002/2013GL058578>

- Chaffin, M. S., Deighan, J., Schneider, N. M., & Stewart, A. I. F. (2017). Elevated atmospheric escape of atomic hydrogen from Mars induced by high-altitude water. *Nature Geoscience*, *10*(3), 174–178. <https://doi.org/10.1038/ngeo2887>
- Chaufray, J.-Y., Bertaux, J.-L., Leblanc, F., & Quémérais, E. (2008). Observation of the hydrogen corona with SPICAM on Mars Express. *Icarus*, *195*(2), 598–613. <https://doi.org/10.1016/j.icarus.2008.01.009>
- Chaufray, J.-Y., Bertaux, J.-L., Quémérais, E., Leblanc, F., & Sulis, S. (2015). Observations of the nightside Venusian hydrogen corona with SPICAV/VEX. *Icarus*, *262*, 1–8. <https://doi.org/10.1016/j.icarus.2015.08.013>
- Chaufray, J.-Y., Bertaux, J.-L., Quémérais, E., Villard, E., & Leblanc, F. (2012). Hydrogen density in the dayside Venusian exosphere derived from Lyman- α observations by SPICAV on Venus Express. *Icarus*, *217*, 767–778. <https://doi.org/10.1016/j.icarus.2011.09.027>
- Chaufray, J.-Y., Gonzalez-Galindo, F., Forget, F., Lopez-Valverde, M. A., Leblanc, F., Modolo, R., & Hess, S. (2015). Variability of the hydrogen in the Martian upper atmosphere as simulated by a 3D atmosphere-exosphere coupling. *Icarus*, *245*, 282–294. <https://doi.org/10.1016/j.icarus.2014.08.038>
- Chaufray, J.-Y., Gonzalez-Galindo, F., Forget, F., Lopez-Valverde, M. A., Leblanc, F., Modolo, R., & Hess, S. (2017). Reply to comment “On the hydrogen escape: Comment to variability of the hydrogen in the Martian upper atmosphere as simulated by a 3D atmosphere-exosphere coupling by J-Y Chaufray et al.” by V. Krasnopolsky. *Icarus*, *301*, 132–135. <https://doi.org/10.1016/j.icarus.2017.07.013>
- Chen, Y., & Cloutier, P. A. (2003). Martian hydrogen exosphere charge exchange by solar wind. *Journal of Geophysical Research*, *108*(A10), 1381. <https://doi.org/10.1029/2002JA009604>
- Clarke, J. T., Mayyasi, M., Bhattacharyya, D., Schneider, N. M., McClintock, W. E., Deighan, J. I., et al. (2017). Variability of D and H in the Martian upper atmosphere observed with the MAVEN IUVS echelle channel. *Journal of Geophysical Research: Space Physics*, *122*, 2336–2344. <https://doi.org/10.1002/2016JA023479>
- Donahue, T. M., & McAfee, J. R. (1964). Influence of lateral flow on the diurnal variation in exospheric hydrogen. *Planetary and Space Science*, *12*(11), 1045–1054. [https://doi.org/10.1016/0032-0633\(64\)90081-9](https://doi.org/10.1016/0032-0633(64)90081-9)
- Elrod, M. K., Bougher, S., Bell, J., Mahaffy, P. R., Benna, M., Stone, S., et al. (2017). He bulge revealed: He and CO₂ diurnal variations in the upper atmosphere of Mars as detected by MAVEN/NGIMS. *Journal of Geophysical Research: Space Physics*, *122*, 2564–2573. <https://doi.org/10.1002/2016JA023482>
- Forget, F., Hourdin, F., Fournier, R., Talagrand, O., Collins, M., et al. (1999). Improved general circulation models of the Martian atmosphere from the surface to above 80 km. *Journal of Geophysical Research*, *104*, 24,155–24,175.
- Gilli, G., Lebonnois, S., Gonzalez-Galindo, F., Lopez-Valverde, M. A., Stolzenbach, M. A., Lefevre, F., et al. (2017). Thermal structure of the upper atmosphere of Venus simulated by a ground to thermosphere GCM. *Icarus*, *281*, 55–72. <https://doi.org/10.1016/j.icarus.2016.09.016>
- Gonzalez-Galindo, F., Forget, F., Lopez-Valverde, M. A., Angelats i Coll, M., & Millour, E. (2009). A ground-to-exosphere Martian general circulation model: 1. Seasonal, diurnal, and solar cycle variation of thermospheric temperatures. *Journal of Geophysical Research*, *114*, E04001. <https://doi.org/10.1029/2008JE003246>
- Gonzalez-Galindo, F., Lopez-Valverde, M. A., Forget, F., Garcia-Comas, M., Millour, E., & Montabone, L. (2015). Variability of the Martian thermosphere during eight Martian years as simulated by a ground-to-exosphere global circulation model. *Journal of Geophysical Research: Planets*, *120*, 2020–2035. <https://doi.org/10.1002/2015JE004925>
- Grebowsky, J. M., Kasprzak, W. T., Hartle, R. E., & Donahue, T. M. (1996). A new look at Venus’ thermosphere H distribution. *Advances in Space Science*, *17*(11), 191–195. [https://doi.org/10.1016/0273-1177\(95\)00749-5](https://doi.org/10.1016/0273-1177(95)00749-5)
- Hodges, R. R., & Johnson, F. S. (1968). Lateral transport in planetary exospheres. *Journal of Geophysical Research*, *73*(23), 7307–7317. <https://doi.org/10.1029/JA073i023p07307>
- Holmstrom, M. (2006). Asymmetries in Mars’ exosphere: Implications for X-ray and ENA imaging. *Space Science Reviews*, *126*(1–4), 435–445. <https://doi.org/10.1007/s11214-006-9036-7>
- Huebner, W. F., Keady, J. J., & Lyon, S. P. (1992). Solar photo rates for planetary atmospheres and atmospheric pollutants. *Astrophysics and Space Science*, *195*(1), 1–294. <https://doi.org/10.1007/BF00644558>
- Johnson, F. S., & Gottlieb, B. (1969). Composition change in the lower atmosphere. *Space Research*, *9*, 442.
- Krasnopolsky, V. A. (2010). Solar activity variations of thermospheric temperatures on Mars and a problem of CO in the lower atmosphere. *Icarus*, *207*, 618–647.
- Kumar, S., Hunten, D. M., & Broadfoot, A. L. (1978). Non-thermal hydrogen in the Venus exosphere: The ionospheric source and the hydrogen budget. *Planetary and Space Science*, *26*(11), 1063–1075. [https://doi.org/10.1016/0032-0633\(78\)90029-6](https://doi.org/10.1016/0032-0633(78)90029-6)
- Leblanc, F., Chaufray, J.-Y., Modolo, R., Leclercq, L., Curry, S., Luhmann, J., et al. (2017). On the origins of Mars’ exospheric nonthermal oxygen component as observed by MAVEN and modeled by Heliosares. *Journal of Geophysical Research: Planets*, *122*, 2401–2428. <https://doi.org/10.1002/2017JE005336>
- Lewkow, N. R., & Kharchenko, V. (2014). Precipitation of energetic neutral atom and induced non-thermal escape fluxes from the Martian atmosphere. *The Astrophysical Journal*, *790*(2), 98. <https://doi.org/10.1088/0004-637X/790/2/98>
- McAfee, J. R. (1967). Lateral flow in the exosphere. *Planetary and Space Science*, *15*, 599–609.
- Maltagliati, L., Montmessin, F., Korablev, O., Fedorova, A., Forget, F., Määttänen, A., et al. (2013). Annual survey of water vapor vertical distribution and water-aerosol coupling in the Martian atmosphere observed by SPICAM/Mex solar occultations. *Icarus*, *223*(2), 942–962. <https://doi.org/10.1016/j.icarus.2012.12.012>
- Modolo, R., Chantaur, G. M., Dubinin, E., & Matthews, A. P. (2005). Influence of the solar activity on the Martian plasma environment. *Annales de Geophysique*, *23*(2), 433–444. <https://doi.org/10.5194/angeo-23-433-2005>
- Navarro, T., Madeleine, J.-B., Forget, F., Spiga, A., Millour, E., Montmessin, F., & Määttänen, A. (2014). Global climate modeling of the Martian water cycle with improved microphysics and radiatively active water ice clouds. *Journal of Geophysical Research: Planets*, *119*, 1479–1495. <https://doi.org/10.1002/2013JE004550>
- Niemann, H. B., Kasprzak, W. T., Hedin, A. E., Hunten, D. M., & Spencer, N. W. (1980). Mass spectroscopic measurements of the neutral gas composition of the thermosphere and exosphere of Venus. *Journal of Geophysical Research*, *85*, 7841.
- Reber, C. A., & Hays, P. B. (1973). Thermospheric wind effects on the distribution of helium and argon in the Earth’s upper atmosphere. *Journal of Geophysical Research*, *78*(16), 2977–2991. <https://doi.org/10.1029/JA078i016p02977>
- Stone, S., Yelle, R., Mahaffy, P., Benna, M., Elrod, M., & Bougher, S. (2016). Temperature variations in the Martian atmosphere from MAVEN NGIMS, DPS meeting, Pasadena, Abstract 303.08
- Terada, K., Terada, N., Shinagawa, H., Fujiwara, H., Kasaba, Y., Seki, K., et al. (2016). A full-particle Martian upper thermosphere-exosphere model using the DSMC method. *Journal of Geophysical Research: Planet*, *121*, 1429–1444. <https://doi.org/10.1002/2015JE004961>
- Vidal-Madjar, A., & Bertaux, J.-L. (1972). A calculated hydrogen distribution in the exosphere. *Planetary and Space Science*, *20*(8), 1147–1162. [https://doi.org/10.1016/0032-0633\(72\)90004-9](https://doi.org/10.1016/0032-0633(72)90004-9)